Article
Self-powered carbon-neutral system

Wen Wang (王文), Shengwei Zhang (张声威), Qi Liu (刘琦), ..., Cong Liu (刘聪), Zhong Lin Wang (王中林), Dan Luo (罗聃)

liucong@binn.cas.cn (C.L.)
zhong.wang@mse.gatech.edu (Z.L.W.)
luodan@binn.cas.cn (D.L.)

Highlights

A self-powered carbon-neutral system was proposed to mitigate carbon emissions

TENG-EMG could convert the kinetic energy of flue gases into electricity for eCO_2RR

The Faraday efficiency of ethanol conversion could reach as high as 70.77% at −0.5 V

CA could effectively capture CO_2 from flue gases as feedstock for eCO_2RR

The electrocatalytic CO_2 reduction is a promising option for achieving carbon neutrality and mitigating climate change. However, the electricity used for the eCO_2RR is mainly derived from gray electricity. Here, Wang et al. propose a self-driven carbon-neutral system for industrial exhaust gases, which can effectively reduce the CO_2 emissions.

Cell Reports
Physical Science

 CellPress

Article

Self-powered carbon-neutral system

Wen Wang (王文),[1,2,5] Shengwei Zhang (张声威),[2,5] Qi Liu (刘琦),[3,5] Yuan Bai (白源),[1,2] Tao Jiang (蒋涛),[2] Bowen Guo (郭博文),[2,3] Cong Liu (刘聪),[2,*] Zhong Lin Wang (王中林),[2,4,*] and Dan Luo (罗聃)[2,6,*]

SUMMARY

A carbon capture and utilization strategy, especially the electrocatalytic CO_2 reduction reaction (eCO_2RR), is a promising option for achieving carbon neutrality and mitigating climate change. However, currently, the electricity employed for the eCO_2RR is mainly derived from gray electricity, and it is often difficult to offset the carbon emissions from power generation of the eCO_2RR, which cannot truly achieve carbon neutrality. To circumvent these issues, a self-powered carbon-neutral system integrating the triboelectric nanogenerator-electromagnetic generator (TENG-EMG) with the eCO_2RR for industrial exhaust gases is constructed. In this system, the TENG-EMG-based composite generator can convert the kinetic energy of industrial flue gases into green electricity. Subsequently, single-atom copper catalysts can efficiently utilize the electricity generated by generators to realize a remarkably high Faraday efficiency for ethanol. In sharp contrast to traditional eCO_2RRs, a self-driven carbon-neutral system can dramatically reduce the costs of generating and transmitting electricity and can truly achieve zero or even negative carbon emissions.

INTRODUCTION

Since the first industrial revolution, overexploitation and excessive use of fossil fuels have significantly increased CO_2 emissions, contributing to global warming and climate change.[1–3] In order to limit the rise of global temperature, tremendous efforts have been devoted to mitigating the CO_2 accumulation in the atmosphere for carbon neutrality.[4–8] Currently, the carbon capture and storage (CCS) strategy has been regarded as a major climate change mitigation option for carbon neutrality, focusing on storing captured CO_2 in deep geological structures.[9] Nevertheless, the CCS strategy is confronted with the following critical issues: extra energy input in the desorption and compression of CO_2 and the potential acidification and damage of soil, as well as geological structure changes, possibly even leading to earthquakes.[10,11] To circumvent the existing matters, a carbon capture and utilization (CCU) strategy has been proposed, combining CO_2 emission reduction with fuel/chemical conversion, and thereby is gaining attention as a promising method in the long term.[12–14] However, the current means and technologies are not yet mature, and there are many challenges mainly related to technology and cost issues that need to be solved.[12,15] Thus, it is still necessary to explore a more economical and efficient CCU strategy to achieve carbon neutrality.

Currently, the realization of a low-carbon energy system through the catalytic CO_2 reduction reaction (CO_2RR) is a realistic CCU path to reduce CO_2 emissions and advance the carbon-neutral process. Specially, the CO_2RR has been facilitated by numerous techniques, including electrocatalysis,[16–18] thermocatalysis,[19,20]

[1]School of Chemistry and Chemical Engineering, Guangxi University, Nanning 530004, China

[2]Beijing Institute of Nanoenergy and Nanosystems, Chinese Academy of Sciences, Beijing 101400, China

[3]Unconventional Petroleum Research Institute, China University of Petroleum, Beijing 100049, China
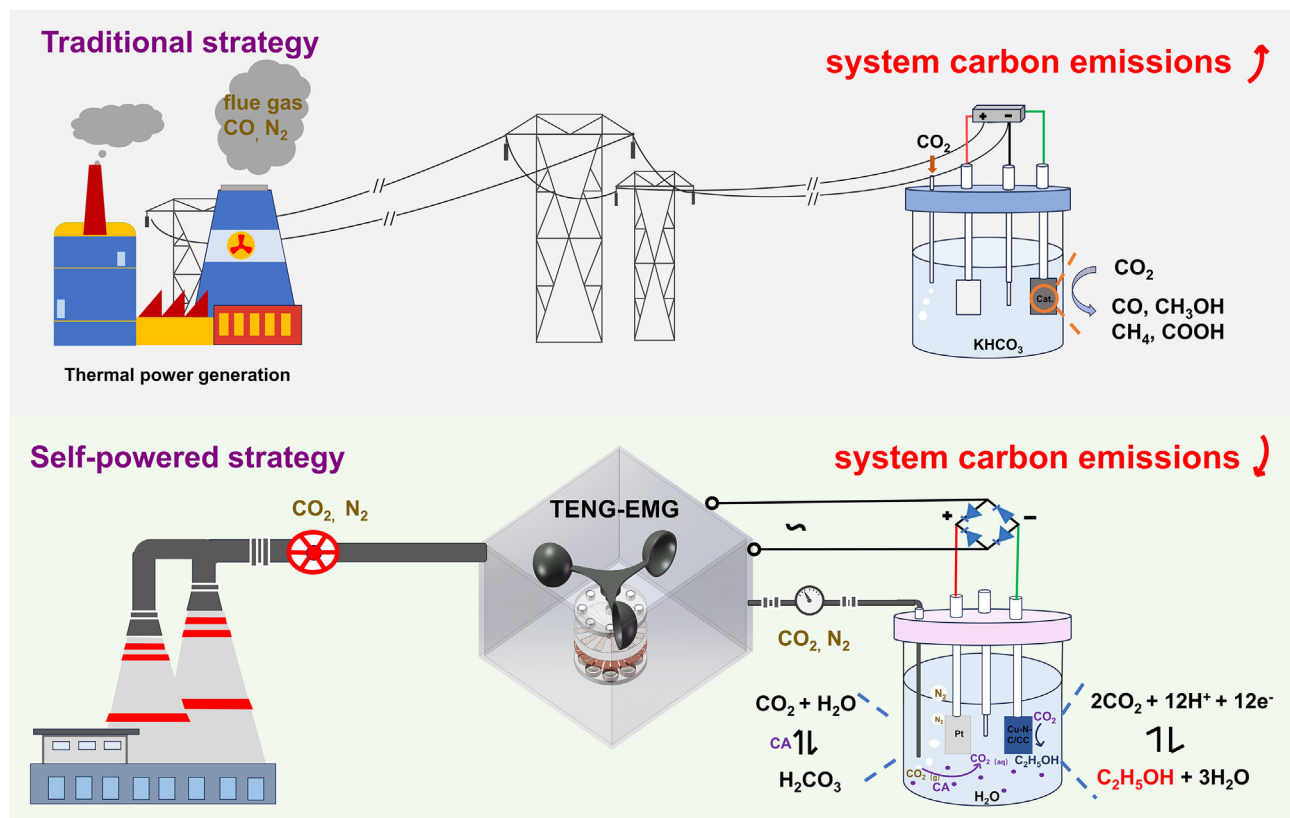
[4]Georgia Institute of Technology, Atlanta, GA 30332-0245, USA

[5]These authors contributed equally

[6]Lead contact

*Correspondence: liucong@binn.cas.cn (C.L.), zhong.wang@mse.gatech.edu (Z.L.W.), luodan@binn.cas.cn (D.L.)

https://doi.org/10.1016/j.xcrp.2024.101871

Scheme 1. Illustration of traditional and self-powered carbon-neutral system

Traditional strategy: eCO_2RR was mostly driven by dirty electrical energy from thermal power generation, leading to a sharp increase in cost and system carbon emissions. Self-powered strategy: eCO_2RR was *in situ* operated by a self-driven TENG-EMG from the conversion of kinetic energy into electrical energy, achieving negative system carbon emissions and an ideal carbon-neutral process.

photocatalysis,[21–23] and bioconversion.[24,25] Due to its special benefits, including flexible electricity, mild reaction conditions, straightforward reaction unit, and enormous potential for practical industrial applications, the electrocatalytic CO_2RR (eCO_2RR) is one of the most promising strategies to achieve carbon-neutral goals.[26–28] To date, numerous catalysts have been developed for the eCO_2RR, among which copper-based catalysts, especially single-atom copper catalysts, have been proved to be the most potential catalysts. However, the eCO_2RR is mostly driven by gray electricity from thermal power generation in the traditional strategy, leading to a sharp increase in cost and system carbon emissions. In addition, it is often difficult to offset the carbon emissions from power generation of the CO_2 conversion by electrocatalytic reduction in the traditional strategy, which cannot truly achieve carbon neutrality (Scheme 1). The traditional eCO_2RR strategy further highlights that the major challenge to the reduction in cost and carbon emissions is to produce the required carbon-free electricity at very low cost. Originating from Maxwell's displacement current, triboelectric nanogenerators (TENGs) with simple fabrication, high energy conversion efficiency, and low cost were first proposed in 2012.[29] Technologically, TENGs were considered as one of the most promising and environmentally friendly energy conversion techniques, harvesting ambient mechanical energy to produce large quantities of zero-carbon electricity with high availability and low cost for self-powered applications.[30,31] In addition, TENGs are typically characterized by high voltage and low current, while the electromagnetic generator (EMG) is characterized by high current and low voltage.[32] Combining

Cell Reports
Physical Science
Article

CellPress

the complementary strengths of TENGs and EMGs,[33,34] the TENG-EMG not only improves the energy harvesting efficiency and widens the energy harvesting range but also expands the range of self-powered system applications. In contrast to the traditional strategy, CCU systems integrating eCO_2RR and TENG-EMG techniques can be identified as a potential enabling platform technology to mitigate carbon emissions economically and efficiently for carbon-neutral goals.

Herein, integrating the TENG-EMG composite generator and the eCO_2RR device, a self-powered carbon-neutral system is constructed, as shown in Scheme 1, which is realized by a self-driven and *in situ* eCO_2RR. In this work, the continuous flow of flue gas passes through the TENG-EMG device and then can lead to the conversion of kinetic energy into green electricity over a wide operating range and a wide range of wind speeds, offering zero-carbon electricity with high availability and low cost in a carbon-neutral system. Specially, a single-atom copper catalyst with a remarkably high Faraday efficiency for ethanol and an electrolyte solution containing carbonic anhydrase (CA) with excellent ability to capture low concentrations of CO_2 are employed in this system, and the CO_2 conversion efficiency is much better than that of the conventional $KHCO_3$ solution, achieving economical and efficient CCU. In contrast to the conventional strategy with a sharp increase in cost and system carbon emissions, this self-powered carbon-neutral system integrating a self-driven TENG-EMG and *in situ* eCO_2RR can effectively achieve zero or negative system carbon emissions.

RESULTS AND DISCUSSION

Principles and performance of compound generators

The structure of the TENG-EMG device for self-powered CO_2 reduction is illustrated in Figure 1A and consists mainly of two components: the stator and the rotor. The stator was composed of nylon, metal electrodes, copper coils, and acrylic plates. For the TENG section, 24 aluminum electrodes were connected to the stator at intervals, and a layer of nylon was attached to increase the voltage. For the EMG section, 8 copper coils were evenly embedded at the edge of the stator. The rotor was an acrylic plate with 8 magnets of the same polarity embedded inside and 12 sector polytetrafluoroethylene (PTFE) film adhered to the surface. The rotor was connected to the cup, allowing it to rotate with the cup. There was a small gap between the rotor and stator to reduce frictional resistance when rotating at high speeds.

The power generation principle of the non-contact-sliding freestanding mode TENG-EMG in the short-circuit state is shown in Figures 1B and 1C. For the TENG part, due to electrostatic induction in the initial state (Figures 1B–1Bi), equal amounts of positive and negative charges were induced on the left and right electrodes, at which time the left electrode was negatively charged, the right electrode was positively charged, and the potential difference between the two electrodes was at its maximum. As the PTFE film rotated, the charge on the left electrode was transferred to the right electrode through an external circuit (Figures 1B–1Bii), and when the potential of the right electrode was lower than that of the left electrode, the direction of the current in the circuit was reversed (Figures 1B–1Biii). The entire cycle of the power generation process was completed when the PTFE rotated to the position where the left electrode in the second pair overlapped (Figures 1B–1Biv). Thus, the periodic potential difference would continue to drive electrons to transfer between the two sets of electrodes when the rotor remains rotating, creating a continuous AC output. For the EMG part, in the initial state, the coil was located below the magnet (Figures 1C–1Ci), and when the magnet started to rotate, the distance between the
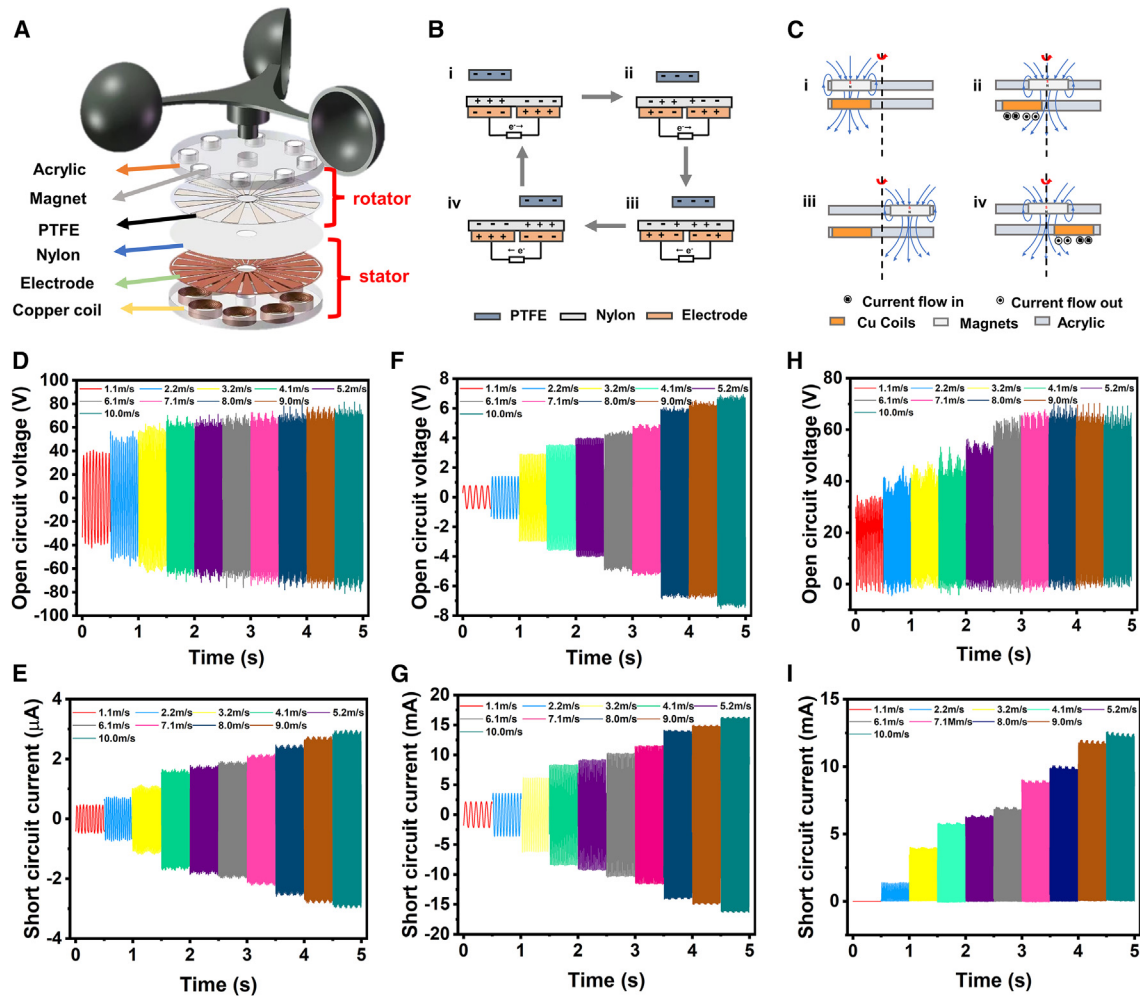
Figure 1. Construction of TENG-EMG
(A) Illustration of the TENG-EMG model.
(B) Working principle of the TENG.
(C) Working principle of the EMG.
(D) Open-circuit voltage of TENG.
(E) Short-circuit current of TENG.
(F) Open-circuit voltage of EMG.
(G) Short-circuit current of EMG.
(H) Open-circuit voltage of TENG-EMG.
(I) Short-circuit current of TENG-EMG.

magnet and the coil changed, the magnetic flux changed, and an induced current was generated in the copper coil (Figures 1C–1Cii). When the magnet and coil were completely separated, no magnetic flux passed through the coil, and there was no current at this point (Figures 1C–1Ciii). As the magnet continued to rotate, the magnetic flux in the second coil gradually increased, at which point the magnetic inductance was reversed and the direction of the flux was reversed, generating a reverse current (Figures 1C–1Civ). Thus, when the rotor was kept rotating, a periodic alternating current was generated due to the periodic change in magnetic flux.

During the operation of the TENG-EMG, an air pump was used as an analog drive to measure the wind speed with an anemometer and the basic performance of the

**Cell Reports
Physical Science**
Article

generator with an oscilloscope and an electrostatic meter. As shown in Figures 1D and 1E, both the TENG short-circuit current (Isc) and open-circuit voltage (Voc) increased gradually with the increase of wind speed. The rapid increase in voltage in the first period was due to the fact that the surface charge has not yet reached saturation, and when the surface charge reaches saturation, the voltage no longer increases. Besides, both Isc and Voc of the EMG increased with the increase in wind speed (Figures 1F and 1G). When the TENG and the EMG were rectified and connected in parallel, their Isc and Voc values also increased with the increase of wind speed. When the wind speed reached 10 m/s, the current and voltage of the composite generator (TENG-EMG) reached 13.37 mA and 66.22 V, respectively (Figures 1H and 1I). Based on in-depth analysis of the above data, it is worth noting that the voltage of the TENG-EMG mainly originated from the TENG, while the current mainly originated from the EMG, which results in a good current-voltage output of the TENG-EMG (Figure S1). In addition, we explored the electrical output of the TENG and the EMG at 5 m/s with different external loads (Figures S2). When variable external loads were connected to the TENG and the EMG, the output voltage increased with the load resistance, while the output current was the opposite, and the output power first increased and then decreased with the resistance. The charging curves of different capacitors (10, 22, and 33 μF) at a wind speed of 5 m/s in Figures S3A show that the smaller the rated capacity of the capacitor, the shorter the charging time, and the charging curves of capacitors with capacitance of 10 μF at different rotational speeds (5, 7, and 9 m/s) in Figures S3B show that the charging rate increased with the increase in rotational speed.

To evaluate the performance of the TENG-EMG in different simulated flue gas environments, the effects of variable relative humidity, temperature, and gas components on the TENG-EMG at a constant wind speed of 5 m/s were also explored. As shown in Figure 2A, it could be found that the relative humidity further increased from 23% to 92% and that the voltage decreased from 60.72 to 37.13 V, indicating that the voltage of the TENG-EMG decreased with the increase of relative humidity. On the other hand, the current of the TENG-EMG was maintained around 6.47 mA (Figure 2B). which might be a result of the fact that the voltage of the TENG-EMG mainly originated from the TENG, while the current mainly originated from the EMG. As the humidity increased, a large amount of water accumulated on the PTFE surface, which might lead to the formation of a water molecule layer on the PTFE surface and promote charge dissipation, further resulting in a decrease in electrical output.[35] As shown in Figure 2C, the voltage of the TENG-EMG increased at the beginning and then remained constant when the temperature was increased from 28°C to 60°C. This is due to the fact that the relative humidity also changed during the process of temperature increase, which decreased from 23% to 8%, while the current of the TENG-EMG gradually decreased from 6.17 to 5.06 mA with the temperature increase (Figure 2D), which was due to the fact that as the temperature increased, the magnetic susceptibility decreased, leading to the decrease of current. The humidity of the factory flue gas was about 20%, and the temperature was 50°C. Under this condition, the output of the TENG-EMG was still high enough to satisfy the catalytic condition (Figures 2E and 2F). Besides, it could be seen that the different gas components had almost no effect on the output of the TENG-EMG, which showed that the TENG-EMG was able to maintain a stable output under the condition of a flue gas environment.

Characterization and performance of catalysts

Nanostructured copper single-atom catalyst electrodes were prepared on carbon cloth by a three-step procedure as shown in Figure 3A. Firstly, zeolite imidazolium
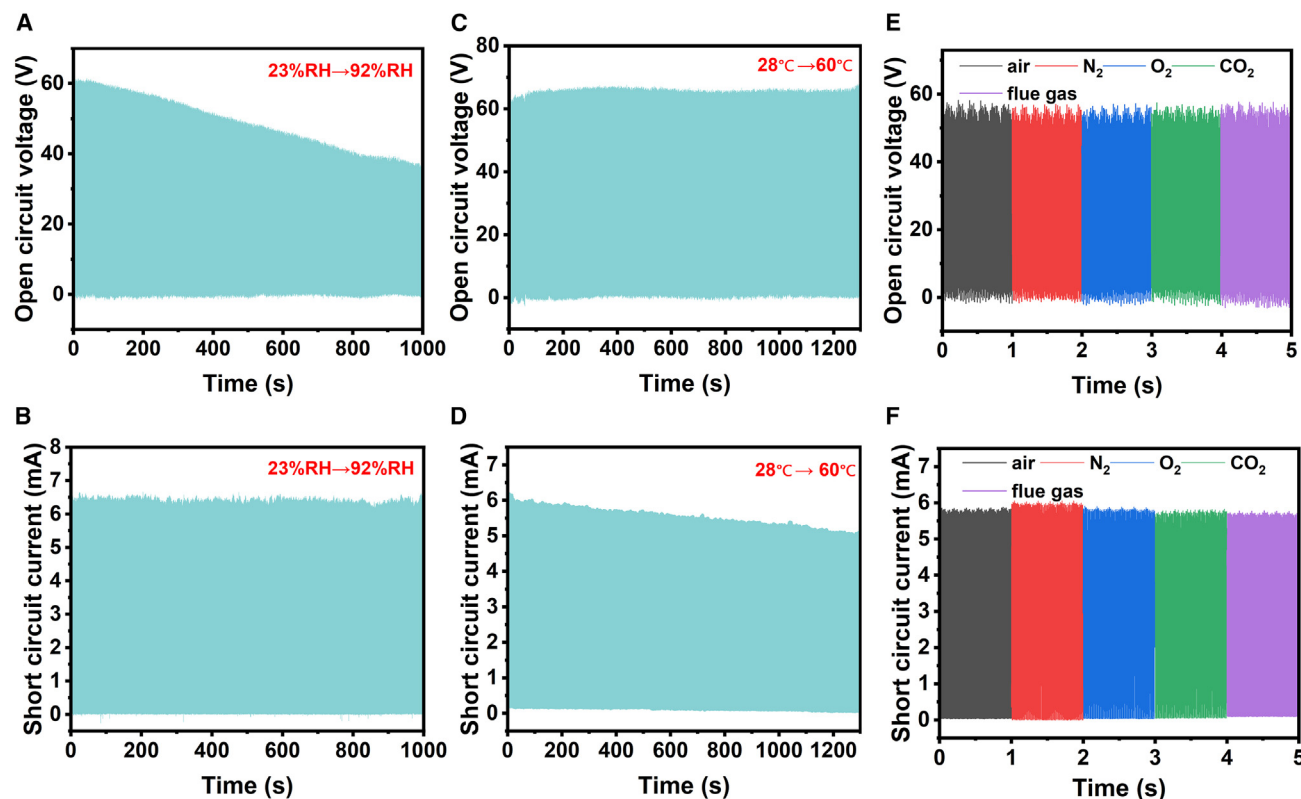
Figure 2. Performance evaluation of TENG-EMG in different flue gas environments
(A and B) Voc (A) and Isc (B) of the wind-driven flexible TENG-EMG versus variable humidity gradients (wind speed: 5 m/s).
(C and D) Voc (C) and Isc (D) of the wind-driven flexible TENG-EMG versus variable temperature (relative humidity [RH]: 23%, wind speed: 5 m/s).
(E and F) Voc (E) and Isc (F) of the wind-driven flexible TENG-EMG versus variable gas composition. (RH: 23%, wind speed: 5 m/s).

skeleton (ZIF-8) arrays were grown *in situ* on the carbon cloth (CC) as precursors. Then, Zn was volatilized by pyrolysis treatment to generate N-doped C (N-C) nano-arrays. Finally, Cu-N-C/CC was obtained by impregnation and pyrolysis treatment to anchor the Cu atoms to the N-C. In order to obtain better CO_2 electrocatalytic reduction performance, we tried to change its electrocatalytic performance by controlling the impregnation concentration. Single-atom catalysts with different amounts of Cu were selectively prepared and named Cu-N-C-0.5, Cu-N-C-1.5, and Cu-N-C-2.5, respectively. Scanning electron microscopy characterization of the three catalysts was performed to show that all of them retained the pristine nanosheet array features (Figures 3B, 3C, S4, and S5). The aberration-corrected high-angle annular dark-field scanning transmission electron microscopy (TEM) showed that the dense bright spots in the N-C matrix were uniformly dispersed in the form of single atoms without observation of metal nanoparticles (Figure 3D). Energy-dispersive X-ray spectroscopy analysis confirmed that Cu and N elements were uniformly distributed on the nanosheets (Figure 3E).

For the structure of Cu-N-C-1.5, Raman spectra in Figure 3F showed the presence of D and G bands in all three catalysts, and Cu-N-C-1.5 exhibited the smallest I_D/I_G with a ratio of 1.2194, which implied the maximum degree of graphitization in Cu-N-C-1.5.[36–38] Then, X-ray diffraction patterns, illustrated in Figure 3G, demonstrated that no characteristic peaks attributed to Cu or Cu oxide nanocrystals were detected and that only broad diffraction peaks attributed to the (002) and (100) planes of
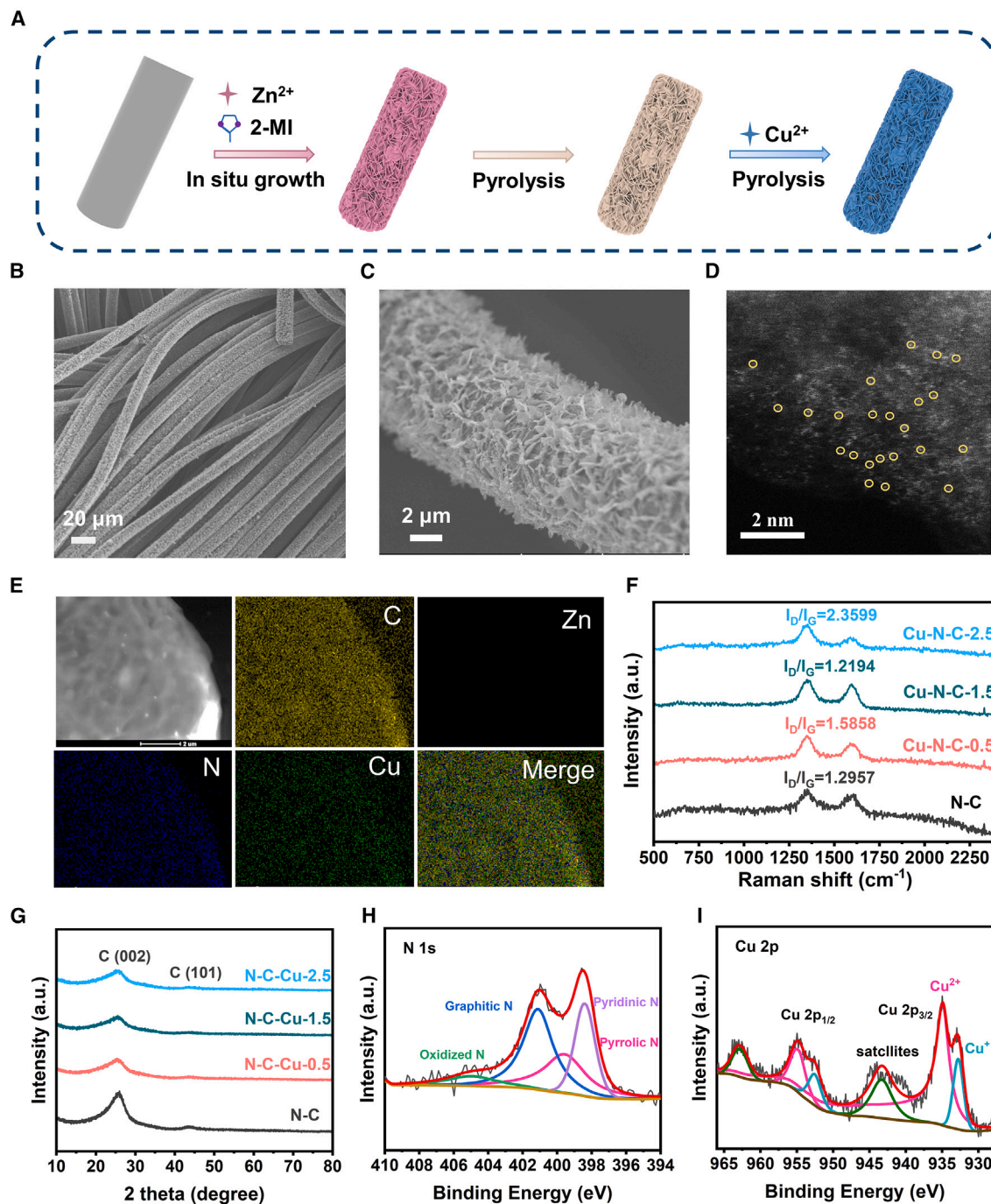
Figure 3. Synthesis and characterization of catalysts

(A) Illustration for the preparation of Cu-N-C/CC.

(B and C) Scanning electron microscopy (SEM) of Cu-N-C-1.5.

(D) Aberration-corrected high-angle annular dark-field (HAADF)-STEM.

(E) Elemental mapping of Cu-N-C-1.5.

(F) Raman spectra of three catalysts.

(G) X-ray diffraction (XRD) patterns of three catalysts.

(H) High-resolution XPS spectra of N 1s of Cu-N-C-1.5.

(I) High-resolution XPS spectra of Cu 2p of Cu-N-C-1.5.
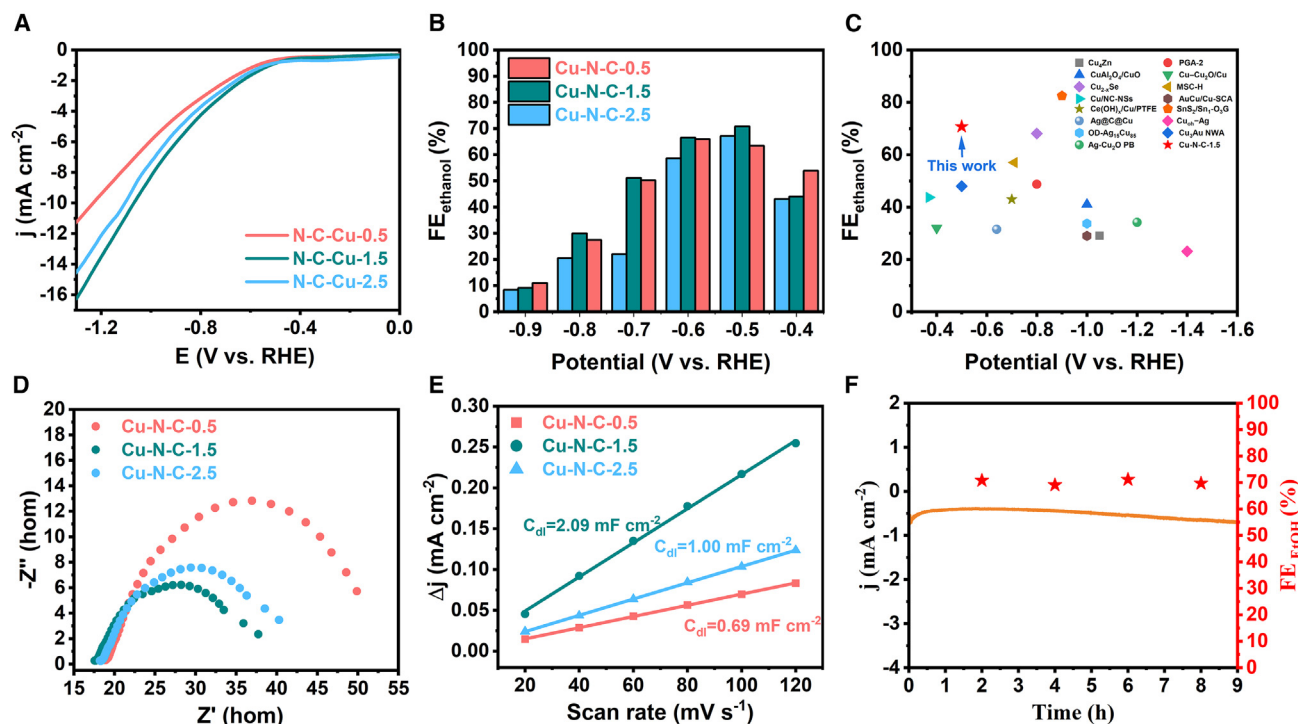
Figure 4. eCO$_2$RR performance of catalysts
(A) LSV curves recorded in CO$_2$-saturated 0.1 M KHCO$_3$ solution using three catalysts.
(B) FE of ethanol obtained at different applied potentials.
(C) Comparison of the eCO$_2$RR performance to ethanol of the recently reported Cu-based catalysts. See also Table S1.
(D) Electrochemical impedance spectroscopy (EIS) spectra of Cu-N-C-x catalysts.
(E) ECSA of Cu-N-C-x catalysts.
(F) Long-term tests of Cu-N-C-1.5 performed at −0.5 V versus RHE.

carbon were observed, which agrees well with the high-resolution TEM result. Subsequently, X-ray photoelectron spectroscopy (XPS) was used to examine the N and Cu chemical composition of the Cu-N-C series samples. High-resolution N 1s spectra indicated the presence of pyridine N (398.4 eV), pyrrole N (400.8 eV), graphite N (401.2 eV), and oxidized N (403.1 eV) (Figures 3H and S6). In the high-resolution Cu 2p spectra, the binding energies of Cu 2p were located at 934.8 and 932.3 eV, attributed to Cu^{2+} and Cu^{+}, respectively, which further indicated that there was no presence of Cu nanoparticles (Figures 3I and S6).[39]

The eCO$_2$RR performance of Cu-N-C-x (x = 0.5, 1.5, and 2.5) was examined in a conventional three-electrode single-compartment cell with 0.1 M KHCO$_3$ as electrolyte. Linear sweep voltammetry (LSV) curves showed that all the samples had lower current densities in the CO$_2$-saturated electrolyte than in the N$_2$-saturated one, indicating that CO$_2$ was involved in the reaction (Figure S7). In comparison to Cu-N-C-0.5 (−9.43 mA cm^{-2}) and Cu-N-C-2.5 (−12.15 mA cm^{-2}) at −1.2 V versus reversible hydrogen electrode (RHE), the total geometric current density measured for Cu-N-C-1.5 was greater, reaching −13.57 mA cm^{-2} (Figure 4A). This indicated that the Cu-N-C-1.5 catalyst had a faster electron transfer and better eCO$_2$RR performance. Although the Cu-N-C-x catalysts all exhibited similar onset potentials, the Tafel slope of Cu-N-C-1.5 (361.48 mV dec^{-1}) was much smaller than those of Cu-N-C-0.5 (426.15 mV dec^{-1}) and Cu-N-C-2.5 (411.74 mV dec^{-1}), indicating that the reaction kinetics of Cu-N-C-1.5 was much faster than the remaining two catalysts at the smaller Tafel slope (Figure S7). Using Pt as the

anode and AgCl as the reference electrode, Cu-N-C-x could be directly used as the cathode for practical electrolysis due to its good conductivity. After continuous purging of CO_2 gas into the electrolytic cell and electrolysis at a constant potential point for 3 h, C_2H_5OH was detected to be the major eCO_2RR product of Cu-N-C-x. The Faraday efficiency (FE) relative to different potentials of C_2H_5OH is plotted in Figures 4B and S8, and it was clear that all three catalysts produced C_2H_5OH over a range of applied potentials versus RHE from −0.4 to −0.9 V. The ethanol production FE of Cu-N-C-1.5 at −0.5 V was 70.77%, which was higher than Cu-N-C-0.5 (63.39%) and Cu-N-C-2.5 (67.15%). Specifically, compared to previous studies of various eCO_2RR catalysts, the Cu-N-C-1.5 catalyst exhibited a remarkably high Faraday efficiency for the electrocatalytic ethanol system (Figure 4C; Table S1). In addition, the electrochemical impedance spectroscopy results showed that the semicircle diameter of Cu-N-C-1.5 was smaller than those of Cu-N-C-0.5 and Cu-N-C-2.5, which indicated the lowest charge transfer resistance (RCT) from the surface to the reactants, which accelerated the electron transfer and thus the formation of favorable intermediates (Figure 4D). To further study the original catalytic activity of the Cu-N-C-x catalysts, the electrochemical active surface area (ECSA) was evaluated by investigating the double-layer capacitance (Figure S9). Notably, the Cu-N-C-1.5 catalyst obtained the largest active surface area (2.09 mF cm^{-2}), which suggested that the catalyst formed a favorable structure and allowed high accessibility to the active sites within it, thus improving the electrocatalytic performance (Figure 4E). Overall, obtaining a larger ESCA and a smaller RCT might be the key factor for the excellent CO_2RR performance of Cu-N-C-1.5. In addition to the electrocatalytic CO_2 reduction activity, it was also important to evaluate its electrochemical stability. A continuous CO_2RR was performed at −0.5 V versus RHE, where the current density and Faraday efficiency of Cu-N-C-1.5 did not show any significant decay during the 9-h-long test period (Figure 4F). The morphological structure of Cu-N-C-1.5 after the stability test was very close to the initial state (Figures S10–S12), which indicated that Cu-N-C-1.5 had good stability.

Nanogenerator-based coupled system for self-powered carbon-neutral system

Based on the above eCO_2RR performance tests, we selected Cu-N-C-1.5 with the highest FE as the catalyst. CA is the most efficient CO_2 hydration catalyst that has been discovered, with a hydration turnover rate of 10^4 to 10^6, and has the advantages of capturing low-concentration CO_2 economically and efficiently. Therefore, CA was chosen as the CO_2 capture agent in our self-powered carbon-neutral system.[40,41] The capture mechanism was shown in Figure S13. Taking advantage of TENG-EMG, the residual kinetic energy of industrial flue gas was converted into electrical energy to drive *in situ* ethanol synthesis, offering zero-carbon electricity with high availability and low cost and reducing carbon emissions. In the nanogenerator-based coupled system (Figure 5A), an air pump was used to simulate the industrial flue gas source, and the flue gas drove the rotation of the wind cups to make the TENG-EMG generate electrical energy used for the eCO_2RR. Subsequently, the flue gas entered the electrolysis cell, and the CA was used to trap CO_2 into an electrolyte, which provided feedstock for the self-powered, *in situ* catalysis. To explore the effect of CA on CO_2 capture in the self-powered carbon-neutral system, $KHCO_3$, an electrolyte commonly used for the eCO_2RR, was used as a comparison. The trapping efficacy of different electrolytes for pure CO_2 and simulated flue gas ($V_{CO2}:V_{N2}$ = 15%:85%) at the same flow rate was first explored. Under both pure CO_2 and flue gas conditions, CA showed the steepest pH line and the fastest rate of pH decrease within the first 30 s of the reaction, which indicated that the CO_2 trapping effect of CA was the best (Figures 5B–5D). Based on the principle of CO_2 capture in the solution, the low concentration of CO_2 (only 15%) in the flue gas conditions was not sufficient to drive the hydrolysis equilibrium of $KHCO_3$
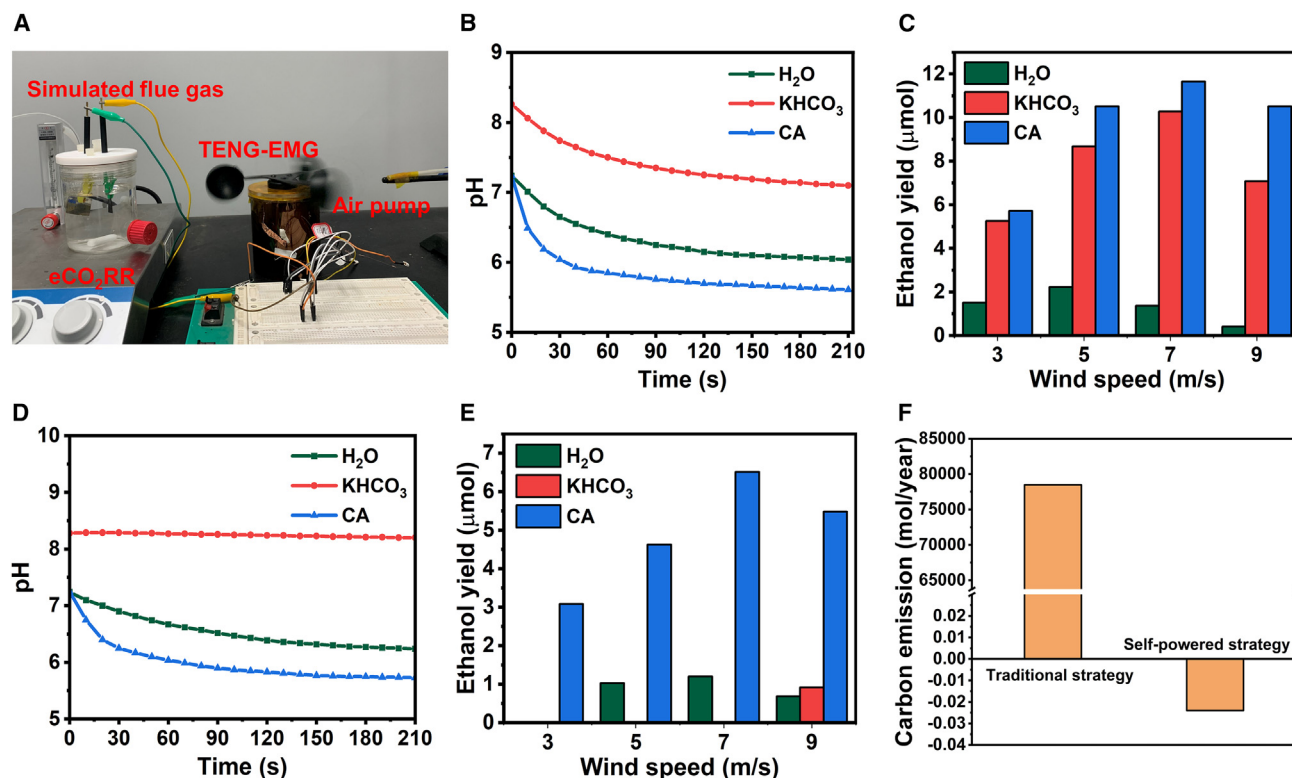
Figure 5. Nanogenerator-based coupled system for self-powered carbon-neutral system
(A) Picture of self-driven electrocatalytic carbon dioxide reduction unit.
(B) Effect of CO_2 gas on solution pH.
(C) Yield of ethanol obtained at different wind speeds (CO_2 gas).
(D) Effect of flue gas on solution pH.
(E) Yield of ethanol obtained at different wind speeds (flue gas).
(F) Statistical calculations of carbon emissions per year of traditional and self-powered strategies. See also Table S2.

to the right, which was reflected by the slight pH change of $KHCO_3$ with time under flue gas conditions (Figure 5D), suggesting that the trapping effect of $KHCO_3$ was not good and that the use of $KHCO_3$ for the construction of an *in situ* eCO_2RR was unsatisfactory in the flue gas. Next, the yield of the eCO_2RR to ethanol under pure CO_2 and flue gas conditions relative to different wind speeds was explored. The self-powered carbon-neutral system was used to produce ethanol successfully after 3 h of reaction under the condition of energized CO_2, and the measured results are shown in Figure 5C. The highest ethanol yield (11.65 µmol) was obtained with the addition of CA as a trapping agent compared to $KHCO_3$ (10.28 µmol) and H_2O (1.37 µmol) at a wind speed of 7 m/s. Under the simulated flue gas flux conditions, the conventional $KHCO_3$ and aqueous solutions were not effective in capturing CO_2, resulting in low ethanol production of 0.912 and 1.20 µmol, respectively (Figure 5E). In stark contrast to the conventional $KHCO_3$ and aqueous solutions as a trapping agent, the ability of CA to effectively capture low concentrations of CO_2 provided favorable conditions for the subsequent CO_2 conversion, resulting in a high ethanol yield of 6.51 µmol. In addition, we also explored the effect of different dosages of CA on electrocatalysis. As shown in Figure S14, more ethanol yield was produced by the eCO_2RR with more CA content. Based on the miniature eCO_2RR process, the self-powered carbon-neutral system integrated self-driven TENG-EMG composite generator and *in situ* eCO_2RR devices resulted in an annual savings of $303 in electricity costs. Besides, rational calculations of carbon emissions (Figure 5F; Table S2) demonstrated that

Cell Reports
Physical Science
Article

CellPress

the self-powered strategy achieved negative system carbon emissions compared to the traditional strategy (78,489 mol/year), which could be a promising way to close the broken carbon cycle and realize the carbon-neutrality goals.

In summary, we designed a self-powered carbon-neutral system integrating a self-driven TENG-EMG and *in situ* eCO$_2$RR to mitigate carbon emissions for carbon neutrality. In this system, the TENG-EMG could convert kinetic energy from industrial exhaust gases into electrical energy for driving the eCO$_2$RR. Surprisingly, by employing a single-atom copper catalyst with a remarkably high Faraday efficiency for ethanol and the electrolyte solution containing CA with excellent ability to capture low concentration of CO$_2$, the CO$_2$ conversion efficiency was much better than that of the conventional KHCO$_3$ solution. Compared to the traditional eCO$_2$RR strategy, the self-powered carbon-neutral system could result in a sharp reduction in electricity-related costs and truly achieve zero or even negative carbon emissions. Considering the implementation of carbon taxes/carbon emission rights, the self-driven carbon-neutral system can not only bring huge economic effects to enterprises but can also play a huge role in breaking the carbon cycle and carbon dioxide stock consumption. Most important of all, due to mitigating climate change of Antarctic glaciers melting, sea levels rising, and desertification areas increasing, the self-driven carbon-neutral system can finally realize the protection of human living areas, as well as win more time for humans to explore human-inhabitable environments in outer space.

EXPERIMENTAL PROCEDURES
Resource availability
Lead contact
Further information and requests for resources and reagents should be directed to and will be fulfilled by the lead contact, Dan Luo (luodan@binn.cas.cn).

Materials availability
This study did not generate new unique materials.

Data and code availability
The authors declare that the data supporting the findings of this study are available within the article and the supplemental information. All other data are available from the lead contact upon reasonable request.

Materials
Zinc nitrate hexahydrate (Zn(NO$_3$)$_2$·6H$_2$O, AR, 99%), 2-methylimidazole (C$_4$H$_6$N$_2$, 98%), methanol (CH$_3$OH, standard for gas chromatography [GC], >99.9%), and copper acetylacetonate (C$_{10}$H$_{14}$CuO$_4$, 97%) were purchased from Shanghai Aladdin Biochemical Technology. Conductive carbon cloth (wos1009/wos1011, CeTech), CA (derived from bovine erythrocytes, Sigma-Aldrich), CO$_2$ and N$_2$ (having a purity of 99.999%), and simulated flue gas (containing 15% CO$_2$ and 85% N$_2$) were provided by Beijing Huanyu Jinghui Jingcheng Gas Technology.

Synthesis
The device mainly consists of a wind cup and a rotating friction-electromagnetic composite nanogenerator. Among them, the composite nanogenerator consists of a stator and a rotor made of circular acrylics. Inside the stator (outer diameter: 90 mm, inner diameter: 13 mm, thickness: 3 mm), 8 circular column grooves were cut, 8 copper coils (inner diameter: 12 mm, outer diameter: 19 mm, height: 2 mm, wire diameter: 0.1 mm) were embedded into the grooves, and 24 fan-shaped aluminum films (outer diameter:

88 mm, thickness: 20 μm) were uniformly affixed to the surface with a spacing of 1 mm and were spaced apart to form the fork-finger electrodes. A layer of nylon (thickness: 25 μm, diameter: 90 mm) was then attached to the surface of the aluminum film as a positive friction layer. Similarly, eight NdFeB magnets (diameter: 12 mm, height: 4 mm) with the same polarity were embedded inside the rotor (diameter: 90 mm, inner diameter: 17 mm, thickness: 5 mm), corresponding to the coils in the stator, and twelve PTFE films of the same size as the fan-shaped aluminum film (thickness: 30 μm) were uniformly attached to the surface of the rotor as a negative friction layer. The rotor was fixed to the air cup, and then the stator was attached to the stainless-steel bearing of the air cup with glue, where the distance between the stator and the rotor was 1 mm. An air pump was used to drive the unit to rotate. The output electrical performance of the H-NG was measured by an electrostatic meter (6517B, Keithley) and an oscilloscope (HDO6104, Teledyne LeCroy).

A typical ZIF-8 nanoarray production process begins with dissolving 594.98 mg $Zn(NO_3)_2 \cdot 6H_2O$ in 40 mL deionized (DI) water, referred to as solution A, and then 1.31 g 2-methylimidazole was dissolved in 40 mL DI water, noted as solution B. Solution B was rapidly poured into solution A and stirred vigorously for 1 min at room temperature. After that, a 2×5 cm^2 piece of clean carbon fabric was etched for 30 min using 0.5 M potassium permanganate, and it was then aged for 2 h in the mixed solution. Subsequently, the carbon cloth was removed and washed several times with DI water and methanol solution and was then dried in an oven at 60°C overnight. Finally, N-C/CC nanosheets were obtained by pyrolysis of ZIF-8 at 800°C (at a heating rate of 1°C/min) for 2 h in N_2 atmosphere.

The precursor N-C/CC was impregnated in a copper solution and then pyrolyzed to yield the Cu-N-C/C/CC catalyst. In a common preparation, 60 mg copper acetylacetonate was dissolved in 40 mL trichloromethane (1.5 mg/mL). A piece of N-C/CC was then immersed in the above solution for 2 h with stirring to allow Cu ions to be absorbed. The carbon cloth was then removed and dried in a vacuum oven at 60°C overnight. Afterward, the samples were heated to 900°C for 2 h under N_2 atmosphere. The heating rate was 5°C/min. The obtained material was labeled as Cu-N-C-1.5 and used directly without further treatment.

A similar procedure to the one previously mentioned was used to synthesize Cu-N-C-0.5 and Cu-N-C-2.5, with the difference being that they were impregnated in different concentrations of Cu solution, i.e., Cu-N-C-0.5 was impregnated in 0.5 mg/mL Cu solution, whereas Cu-N-C-2.5 was impregnated in 2.5 mg/mL Cu solution.

Characterization
Using an SU8020 cold-field scanning electron microscope (Hitachi, Tokyo, Japan) to represent the morphology of the materials. A Tecnai G2 F20 (FEI, Hillsboro, OR, USA) was used for energy-dispersive X-ray spectroscopy and TEM. A LabRAM HR Evolution (confocal microscopy) Raman spectrometer (HORIBA JY, Palaiseau, France) was used to measure the Raman shifts. A Malvern Panalytical Holland xPert 3 powder X-ray diffractometer was used to analyze the samples' crystal structures. XPS was analyzed with Thermo Scientific ESCALAB Xit (Waltham, MA, USA).

Electrochemical measurements
The CHI760E electrochemical workstation (Shanghai Chenhua Instrument, Shanghai, China) was used to conduct all electrochemical measurements in a traditional three-electrode cell. The reference electrode was Ag/AgCl (with saturated KCl as

Cell Reports
Physical Science
Article

CellPress

the filling solution), and the counter electrode was platinum electrode. The working electrode was Cu-N-C/CC (1×1.5 cm^2). For CO_2RR measurements, the electrolyte (200 mL) was purged with CO_2 for 30 min prior to the measurement and at a rate of 50 mL/min. The 0.1 M KHCO$_3$ electrolyte that is saturated with N$_2$ and CO_2 has pH values of 8.6 and 6.8, respectively. In 0.1 M KHCO$_3$ electrolyte, cyclic voltammetry (CV) and LSV were conducted at a scan rate of 20 mV/s. The following formula was used to convert electrode potentials to the RHE: $E_{RHE} = E_{Ag/AgCl} + 0.197$ V $+ 0.0591 \times$ pH. CVs were used to calculate the electrochemical double-layer capacitances. The slope of current versus scan rate is used to compute the ECSA. In the frequency range of 100 kHz to 0.01 Hz, AC impedance measurements were performed at the onset potential with an amplitude of 5 mV.

Faradaic efficiency

The liquid-phase products were detected by GC (GC-7820) after electrolysis at selected potentials for 3 h. Ethanol was detected by flame ionization detector (FID-1). Formic acid was determined by nuclear magnetic resonance spectrometer (Bruker, Leipzig, Germany, 600 MHz) in DMSO. Formaldehyde was detected spectrophotometrically by acetylacetone. FE$_{ethanol}$ was calculated as

$$FE_{ethanol}(\%) = \frac{Q_{ethanol}}{Q_{total}} \times 100\% = \frac{n_{ethanol} \times N \times F}{I \times t} \times 100\%,$$

where n$_{ethanol}$ is the molar amount of ethanol produced in the product. N (= 12) is the number of electrons required to form one ethanol molecule. F is Faraday's constant (96,500 C/mol). I is the steady-state current, and t is the electrolysis time.

SUPPLEMENTAL INFORMATION

Supplemental information can be found online at https://doi.org/10.1016/j.xcrp.2024.101871.

AUTHOR CONTRIBUTIONS

S.Z. and Q.L. conceived the project and designed the experiments. W.W. prepared the samples and performed the electrochemical experiments. Y.B. prepared the TEMG-EMG. B.G. assisted with the partial experiments. Z.L.W. and T.J. assisted with the TEMG-EMG measurements. W.W., C.L., and D.L. analyzed the experimental data and co-wrote the manuscript.

DECLARATION OF INTERESTS

The authors declare no competing interests.

REFERENCES

1. Frölicher, T.L., Fischer, E.M., and Gruber, N. (2018). Marine heatwaves under global warming. Nature *560*, 360–364. https://doi.org/10.1038/s41586-018-0383-9.

2. Rogelj, J., Huppmann, D., Krey, V., Riahi, K., Clarke, L., Gidden, M., Nicholls, Z., and Meinshausen, M. (2019). A new scenario logic for the Paris Agreement long-term temperature goal. Nature *573*, 357–363. https://doi.org/10.1038/s41586-019-1541-4.

3. Supran, G., Rahmstorf, S., and Oreskes, N. (2023). Assessing ExxonMobil's global warming projections. Science *379*, eabk0063. https://doi.org/10.1126/science.abk0063.

4. Lei, T., Wang, D., Yu, X., Ma, S., Zhao, W., Cui, C., Meng, J., Tao, S., and Guan, D. (2023). Global iron and steel plant CO_2 emissions and carbon-neutrality pathways. Nature *622*, 514–520. https://doi.org/10.1038/s41586-023-06486-7.

5. Clery, D. (2006). Global warming. climate changedemands action, says U.K. report. Science *311*, 592. https://doi.org/10.1126/science.311.5761.592b.

6. Pan, H., Page, J., Shi, R., Cong, C., Cai, Z., Barthel, S., Thollander, P., Colding, J., and Kalantari, Z. (2023). Contribution of prioritized urban nature-based solutions allocation to carbon neutrality. Nat. Clim. Chang. *13*, 862–870. https://doi.org/10.1038/s41558-023-01737-x.

7. Kohse-Höinghaus, K. (2023). Combustion, chemistry, and carbon neutrality. Chem. Rev. *123*, 5139–5219. https://doi.org/10.1021/acs.chemrev.2c00828.

8. Zhao, Y., Setzler, B.P., Wang, J., Nash, J., Wang, T., Xu, B., and Yan, Y. (2019). An efficient direct ammonia fuel cell for affordable carbon-neutral transportation. Joule *3*, 2472–2484. https://doi.org/10.1016/j.joule.2019.07.005.

9. Boot-Handford, M.E., Abanades, J.C., Anthony, E.J., Blunt, M.J., Brandani, S., Mac Dowell, N., Fernández, J.R., Ferrari, M.-C., Gross, R., Hallett, J.P., et al. (2014). Carbon capture and storage update. Energy Environ. Sci. *7*, 130–189. https://doi.org/10.1039/c3ee42350f.

10. Bui, M., Adjiman, C.S., Bardow, A., Anthony, E.J., Boston, A., Brown, S., Fennell, P.S., Fuss, S., Galindo, A., Hackett, L.A., et al. (2018). Carbon capture and storage (CCS): the way forward. Energy Environ. Sci. *11*, 1062–1176. https://doi.org/10.1039/c7ee02342a.

11. Sgouridis, S., Carbajales-Dale, M., Csala, D., Chiesa, M., and Bardi, U. (2019). Comparative net energy analysis of renewable electricity and carbon capture and storage. Nat. Energy *4*, 456–465. https://doi.org/10.1038/s41560-019-0365-7.

12. Mac Dowell, N., Fennell, P.S., Shah, N., and Maitland, G.C. (2017). The role of CO_2 capture and utilization in mitigating climate change. Nat. Clim. Chang. *7*, 243–249. https://doi.org/10.1038/nclimate3231.

13. Flores-Granobles, M., and Saeys, M. (2020). Minimizing CO_2 emissions with renewable energy: a comparative study of emerging technologies in the steel industry. Energy Environ. Sci. *13*, 1923–1932. https://doi.org/10.1039/d0ee00787k.

14. Thonemann, N., and Pizzol, M. (2019). Consequential life cycle assessment of carbon capture and utilization technologies within the chemical industry. Energy Environ. Sci. *12*, 2253–2263. https://doi.org/10.1039/c9ee00914k.

15. Abanades, J.C., Rubin, E.S., Mazzotti, M., and Herzog, H.J. (2017). On the climate change mitigation potential of CO_2 conversion to fuels. Energy Environ. Sci. *10*, 2491–2499. https://doi.org/10.1039/c7ee02819a.

16. Zhang, L., Zhang, Y., Hou, Y., Li, H., Li, C., Xin, J., Zhou, N., Li, Q., Song, Y., and Zhang, Z. (2020). Unveiling the active site of metal-free nitrogen-doped carbon for electrocatalytic carbon dioxide reduction. Biomed. Rep. *13*, 8. https://doi.org/10.1016/j.xcrp.2020.100145.

17. Fan, T., Ma, W., Xie, M., Liu, H., Zhang, J., Yang, S., Huang, P., Dong, Y., Chen, Z., and Yi, X. (2021). Achieving high current density for electrocatalytic reduction of CO_2 to formate on bismuth-based catalysts. Cell Rep. Phys. Sci. *2*, 100353. https://doi.org/10.1016/j.xcrp.2021.100353.

18. Yang, Y.L., Wang, Y.R., Dong, L.Z., Li, Q., Zhang, L., Zhou, J., Sun, S.N., Ding, H.M., Chen, Y., Li, S.L., and Lan, Y.Q. (2022). A honeycomb-like porous crystalline hetero-electrocatalyst for efficient electrocatalytic CO_2 reduction. Adv. Mater. *34*, e2206706. https://doi.org/10.1002/adma.202206706.

19. Kang, H., Ma, J., Perathoner, S., Chu, W., Centi, G., and Liu, Y. (2023). Understanding the complexity in bridging thermal and electrocatalytic methanation of CO_2. Chem. Soc. Rev. *52*, 3627–3662. https://doi.org/10.1039/d2cs00214k.

20. Das, S., Pérez-Ramírez, J., Gong, J., Dewangan, N., Hidajat, K., Gates, B.C., and Kawi, S. (2020). Core-shell structured catalysts for thermocatalytic, photocatalytic, and electrocatalytic conversion of CO_2. Chem. Soc. Rev. *49*, 2937–3004. https://doi.org/10.1039/c9cs00713j.

21. Yan, T., Li, N., Wang, L., Liu, Q., Ali, F.M., Wang, L., Xu, Y., Liang, Y., Dai, Y., Huang, B., et al. (2020). How to make an efficient gas-phase heterogeneous CO_2 hydrogenation photocatalyst. Energy Environ. Sci. *13*, 3054–3063. https://doi.org/10.1039/d0ee01124j.

22. Boyjoo, Y., Jin, Y., Li, H., Zhao, G., Guo, H., and Liu, J. (2023). Nanoengineering of photocatalytic electrode materials toward net zero emissions. Cell Rep. Phys. Sci. *4*, 101391. https://doi.org/10.1016/j.xcrp.2023.101391.

23. Liang, J., Yu, H., Shi, J., Li, B., Wu, L., and Wang, M. (2023). Dislocated bilayer MOF enables high-selectivity photocatalytic reduction of CO_2 to CO. Adv. Mater. *35*, e2209814. https://doi.org/10.1002/adma.202209814.

24. Tan, X., and Nielsen, J. (2022). The integration of bio-catalysis and electrocatalysis to produce fuels and chemicals from carbon dioxide. Chem. Soc. Rev. *51*, 4763–4785. https://doi.org/10.1039/d2cs00309k.

25. Weliwatte, N.S., and Minteer, S.D. (2021). Photo-bioelectrocatalytic CO_2 reduction for a circular energy landscape. Joule *5*, 2564–2592. https://doi.org/10.1016/j.joule.2021.08.003.

26. Xu, C., Dong, Y., Zhao, H., and Lei, Y. (2023). CO_2 conversion toward real-world applications: electrocatalysis versus CO_2 batteries. Adv. Funct. Mater. *33*, 32. https://doi.org/10.1002/adfm.202300926.

27. Zhu, D.D., Liu, J.L., and Qiao, S.Z. (2016). Recent advances in inorganic heterogeneous electrocatalysts for reduction of carbon dioxide. Adv. Mater. *28*, 3423–3452. https://doi.org/10.1002/adma.201504766.

28. Zhang, W., Hu, Y., Ma, L., Zhu, G., Wang, Y., Xue, X., Chen, R., Yang, S., and Jin, Z. (2018). Progress and perspective of electrocatalytic CO_2 reduction for renewable carbonaceous fuels and chemicals. Adv. Sci. *5*, 1700275. https://doi.org/10.1002/advs.201700275.

29. Fan, F.-R., Tian, Z.-Q., and Lin Wang, Z. (2012). Flexible triboelectric generator. Nano Energy *1*, 328–334. https://doi.org/10.1016/j.nanoen.2012.01.004.

30. Wang, S., Xu, P., Liu, J., Wang, H., Si, J., Deng, J., Xu, M., and Wang, Z.L. (2023). Underwater triboelectric nanogenerator. Nano Energy *118*, 109018. https://doi.org/10.1016/j.nanoen.2023.109018.

31. Bai, Y., Feng, H., and Li, Z. (2022). Theory and applications of high-voltage triboelectric nanogenerators. Cell Rep. Phys. Sci. *3*, 101108. https://doi.org/10.1016/j.xcrp.2022.101108.

32. Chen, J., Gong, S., Gong, T., Yang, X., and Guo, H. (2023). Stackable direct current triboelectric-electromagnetic hybrid nanogenerator for self-powered air purification and quality monitoring. Adv. Energy Mater. *13*, 5. https://doi.org/10.1002/aenm.202203689.

33. Chen, Y., Cheng, Y., Jie, Y., Cao, X., Wang, N., and Wang, Z.L. (2019). Energy harvesting and wireless power transmission by a hybridized electromagnetic-triboelectric nanogenerator. Energy Environ. Sci. *12*, 2678–2684. https://doi.org/10.1039/c9ee01245a.

34. Yong, S., Wang, H., Lin, Z., Li, X., Zhu, B., Yang, L., Ding, W., Liao, R., Wang, J., and Wang, Z.L. (2022). Environmental self-adaptive wind energy harvesting technology for self-powered system by triboelectric-electromagnetic hybridized nanogenerator with dual-channel power management topology. Adv. Energy Mater. *12*, 43. https://doi.org/10.1002/aenm.202202469.

35. Gao, S., Feng, S., Wang, J., Wu, H., Chen, Y., Zhang, J., Li, Y., Wang, R., Luo, X., Wei, H., and Zeng, X. (2023). Hybridized triboelectric-electromagnetic aeolian vibration generator as a self-powered system for efficient vibration energy harvesting and vibration online monitoring of transmission lines. ACS Appl. Mater. Interfaces *15*, 34764–34778. https://doi.org/10.1021/acsami.3c04588.

CellPress

36. Song, Y., Chen, W., Zhao, C., Li, S., Wei, W., and Sun, Y. (2017). Metal-free nitrogen-doped mesoporous carbon for electroreduction of CO_2 to ethanol. Angew. Chem. Int. Ed. *56*, 10840–10844. https://doi.org/10.1002/anie.201706777.

37. Gao, S., Yang, H., Rao, D., Wang, N., Li, Y., Li, J., Rao, S., Maouche, C., Wu, Z., Li, B., et al. (2022). Supercritical CO_2 assisted synthesis of highly accessible iron single atoms and clusters on nitrogen-doped carbon as efficient oxygen reduction electrocatalysts. Chem. Eng. J. *433*, 134460. https://doi.org/10.1016/j.cej.2021.134460.

38. Xie, W., Li, H., Cui, G., Li, J., Song, Y., Li, S., Zhang, X., Lee, J.Y., Shao, M., and Wei, M. (2021). NiSn atomic pair on an integrated electrode for synergistic electrocatalytic CO_2 reduction. Angew. Chem. Int. Ed. *60*, 7382–7388. https://doi.org/10.1002/anie.202014655.

39. Cao, X., Zhao, L., Wulan, B., Tan, D., Chen, Q., Ma, J., and Zhang, J. (2022). Atomic bridging structure of nickel-nitrogen-carbon for highly efficient electrocatalytic reduction of CO_2. Angew. Chem. Int. Ed. *61*, e202113918. https://doi.org/10.1002/anie.202113918.

40. Cobb, S.J., Badiani, V.M., Dharani, A.M., Wagner, A., Zacarias, S., Oliveira, A.R., Pereira, I.A.C., and Reisner, E. (2022). Fast CO_2 hydration kinetics impair heterogeneous but improve enzymatic CO_2 reduction catalysis. Nat. Chem. *14*, 417–424. https://doi.org/10.1038/s41557-021-00880-2.

41. Ro, Y.H., Kim, K.Y., Jeong, S.K., Rhim, G.B., Moon, D.H., Eo, J., Lee, H.S., Lee, G.W., Lim, B.Y., Chun, D.H., et al. (2023). Membrane-separated reactor for an integrated CO_2 capture-mineralization process using carbonic anhydrase. Chem. Eng. J. *477*, 146847. https://doi.org/10.1016/j.cej.2023.146847.